JOURNAL OF MECHANICAL ENGINEERING AND SCIENCES
ISSN: 2289-4659 e-ISSN: 2231-8380
VOLUME 17, ISSUE 4, 2023, 9663 – 9678
DOI: https://doi.org/10.15282/jmes.17.4.2023.1.0765

RESEARCH ARTICLE

Parametric design of cladding system for tall buildings using computational fluid dynamics approach

L. Colak[1]*, M.N. Balci[2]

[1] Department of Mechancial Engineering, Baskent University, 06790 Ankara, Turkey
Phone: +903122466665; Fax.: +903122466750
[2] Department of Mechanical Engineering, Hacettepe University, 06800 Ankara, Turkey

ABSTRACT - Quasi-static approach in calculation of wind load simply depends on the integration of the fluctuating pressures measured at pressure tubes located at the surface of building models. This approach is suitable to design typical low to medium height buildings. However, for tall buildings, if cladding surface will be designed based on single critical load in a conservative way, it will result in over design and excessive cost phenomena. The main aim of this study is to develop new experimantal and computational procedures to examine surface pressure distribution on tall buildings and to select cladding structure based on different pressure zones, thus in a more efficient way. A tall building is selected, modelled and 1/144 scaled wooden prototype is manufactured. Experimental study is conducted in a wind tunnel at turbulent flow conditions, and pressure values are recorded from tubes assembled on the surface of the prototype. Computational fluid dynamics (CFD) approach is carried out to determine pressure values and $k-\varepsilon$ model is used in turbulent flow. Experimentally and computationally obtained results are observed compatible. After validation, actual wind profile is calculated, scaled and applied to the building model in simulations. Selection of the material thickness for the cladding system is performed parametrically accordint to deflection for elements in prescribed zones based on the computed pressure values. It is shown that new parametric cladding selection method opens up possibility to use less material consumption up to 23.6%, eliminating overdesign with maintaining desired factor of safety, which provides considerable economy on construction costs.

ARTICLE HISTORY
Received : 07th Feb. 2023
Revised : 19th Sept. 2023
Accepted : 24th Nov. 2023
Published : 26th Dec. 2023

KEYWORDS
Wind load
Tall building
Wind tunnel test
Computational fluid dynamics
Parametric cladding design

1.0 INTRODUCTION

Aerodynamic effects should be considered in design of tall buildings because of architectural, structural and environmental concerns. Especially, the number of tall buildings has been increasing in the past two decades due to the overcrowded city centers and decreasing spaces in big cities. First wind tunnel which is capable of creating atmospheric boundary layer with a long test section (15-20 m) was built at Colorado State University in 1962. Wind tunnel tests for the design of World Trade Center in New York were performed there in the mid-1960s [1]. In 1970s, Barriga et al. [2] conducted experimental study to find the pressure distribution on square cylinder at turbulent flow. Roberson and Crowe [3] experimentally determined pressure distribution on a building model under turbulent flow conditions. Cermak [4] studied the influence of wind speed and turbulence profiles on structure's behavior and atmospheric boundary layer was introduced. Several boundary layer wind tunnels (BLWTs) having ability of simulation of different wind profiles were constructed in years between 1980-1995 [4]. Ahmad and Kumar [5] investigated the effect of wind loads on low-rise buildings then authors examined the effect of geometry on wind pressure. Aygun and Baskaya [6] carried out experimental study using wind tunnel to find surface pressure distribution on a high-rise building subjected to wind flow. Authors determined the critical locations in which high pressure exists on the building model. Kim and Kanda [7] examined the mechanism of aerodynamic force reduction on the square plan buildings using wind tunnel tests for fluctuating pressure and fluctuating force. Influences of corner shape and tapering ratio on across-wind response of tall building under suburban and urban flow conditions were investigated. Lin et al. [8] tested nine tall building models with different elevation, aspect ratio and side ratio in wind tunnel to get the effect of these parameters on local wind forces. Cluni et al. [9] carried out a study on wind action on regular and irregular tall buildings. In their study, two methods were used to measure the wind effects called as the high frequency force balance and the synchronous multi-pressure sensing system. Xie [10] studied to improve safety and serviceability of super-tall buildings in strong winds, and aerodynamic optimization of building shapes was reported as the most efficient approach. In this approach, a practical method to assess the effectiveness of three common schemes such as tapering, twisting and stepping of aerodynamic optimization in super-tall building design was proposed. Isyumov et al. [11] conducted experimental study to examine the effect of wind directionality on predicted structural wind loads and cladding pressures on buildings.

Tall buildings have been traditionally constructed as symmetric shapes like rectangular, triangular or circular in plan to avoid seismic induced vibrations due to eccentricity. However, free-style design in plan has been increasing and it leads

*CORRESPONDING AUTHOR | L. Colak | ✉ hussamyahya77@gmail.com

to unconventional design for tall buildings. Advanced vibration control techniques allows designers to construct tall buildings with unconventional complicated shapes, which is useful to reduce wind loads and wind resistant design. Modifying the external shape such as corner modification of the cross-section and tapering along the height are used to reduce wind loads on world's well known tall buildings Taipei 101 and Burj Khalifa. Tanaka et al. [12] investigated the aerodynamic forces and wind pressures acting on tall buildings by a series of experiments with various unconventional shapes involving helical, tilted, tapered and composite types. Kim et al. [13] experimentally analysed the mean and peak pressure coefficients on dome roofs with openings and authors divided dome structure into two zones where cladding structure was designed according to pressure coefficients obtained. Pomaranzi et al. [14] employed wind tunnel tests to examine pressure data for peak cladding load estimation on a high-rise building.

Wong and Chin [15] developed a theoretical model to find wind pressure distribution since wind tunnel tests are not always easily be conducted. In 2013, there was a significant advancement in the calculation of wind pressures due to façade geometry, with a detailed CFD approach [16]. Reda et al. [17] used computational fluid dynamics (CFD) to develop an idealized model in order ro mimic air flow properties in actual cities. McGuill and Keenahan [18] proposed a parametric study using a CFD approach for optimal façade design based on minimization of the force along fin-bracket connection. Ciarlatani et al. [19] used experimental and computational methods to find the peak wind loading on a high-rise building. In order to design the type and thickness of the cladding material, the selection criterion is maximum pressure that cladding material can withstand, where maximum pressure is stagnation of wind on the building. Although stagnation pressures can roughly be estimated by simple Bernoulli equations, the atmospheric boundary layer and blockage effect of the surrounding buildings cannot be resolved by such primitive approach. Wind tunnel testing to assess design loads for cladding structures have been practiced in industry, with the aim of minimizing initial capital costs and more significantly avoiding expensive maintenance costs associated with malfunctions due to leakage and/or structural failure [20]. Since experimental analysis is not always feasible and practical, developing computational model and determination of the most appropriate cladding material type and thickness by using CFD analysis is time and cost effective approach.

Studies mentioned in the foregoing paragraphs is mainly related to the calculation and assessment of wind loads or examination of different geometrical design of tall buildings to reduce wind loadings. However, there is quite limited research which concern mechanical design of cladding structure design based on surface pressures due to wind loading. The main aim of this study is to develop a parametric method to decrease the mass of cladding elements and correspondingly to reduce construction costs. A representative tall building model is selected and its scaled prototype is manufactured. Pressure tubes are assembled on three different sides of the building and surface pressure values are recorded in wind tunnel tests, as shown in Section 2.1. In Section 2.2, a computational model is developed based on computational fluid dynamics (CFD) approach . In Section 3.1, validation of the developed computational model is attained by providing comparison study of pressure values acquired from experimental study and those obtained in CFD simulations for three different air stream velocities. In Section 3.2, the realistic air flow model based on power-law function is applied and surface pressure values are obtained and locations possessing high pressure values are determined. Parametric cladding design is explained as flowcharts and building model is divided into zones from ground to top where each zone has a critical pressure. Wind loads for zones are calculated based on the critical pressure. Cladding elements are designed according to the strength calculations within the allowable deflection limit. This study puts forward a new parametric study which relates obtained surface pressures and wind loads to the strength calculations of cladding elements. Comparison between conventional and parametric selection of cladding elements showed that developed parametric method provides significant economy on material utilization and construction costs without losing safety considerations.

2.0 METHODS

2.1 Experimental Study based on Wind Tunnel Testing

Scaled model of the building is manufactured by wooden materials in the laboratories of mechanical engineering department in Baskent University. Dimensions of the model mock-up are determined considering the wind tunnel dimensions since one of the most important necessities of the wind tunnel tests is that the model dimensions since it must be convenient to the wind tunnel test section [21]. Total height of the prototype building is 115m while total height of the model is 0.8m. Hence, scale factor between the model and prototype is 1/144. Other dimensions of the model are calculated based on this scale factor. In order to get realistic flow distribution, the adjacent structures around the building model are also considered since neighboring buildings have considerable effect on flow [22]. Kayışoğlu et al. [23] performed wind tunnel tests with varying angle of attack, turbulence intensity and vortex shedding to estimate the wind loads on tall buildings. Authors created atmospheric boundary layer by passive surface roughness elements due to shortness of tunnel test section. The wind characteristics data are obtained from the State Meteorological Institute of Turkey for the concerned region. Critical conditions are considered to be the highest wind speed of 25 m/s, which was recorded in 1984. This value is used as the free stream velocity in the wind tunnel tests and boundary condition for the CFD analysis. Tests were performed in one direction (South East-SE) with three different wind velocities- (6 m/s, 12 m/s and 25 m/s). The orientation of the tall building model is illustrated in Figure 1.

Experimental analyses are performed in TÜBİTAK-SAGE (The Scientific and Technological Research Council of Turkey) Ankara Wind Tunnel (AWT). The AWT is a subsonic closed-circuit wind tunnel with the test chamber dimensions of 3.05 m x 2.44 m x 6.10 m. Although this wind tunnel is not a boundary layer wind tunnel (BLWT) with a

long test section, relatively short test room (6.10 m) enables wind tunnel testing for many aeronautical and automotive projects. Atmospheric boundary layer creation can be possible using passive devices or surface roughness elements such as cubes and spires [23, 24]. The 750 kW fan can provide free stream velocities up to 90 m/s in the test area. Temperature is $T = 300\ K$ and air density is measured as $\rho_{air} = 1.1241\ \mathrm{kg/m^3}$ at test section.

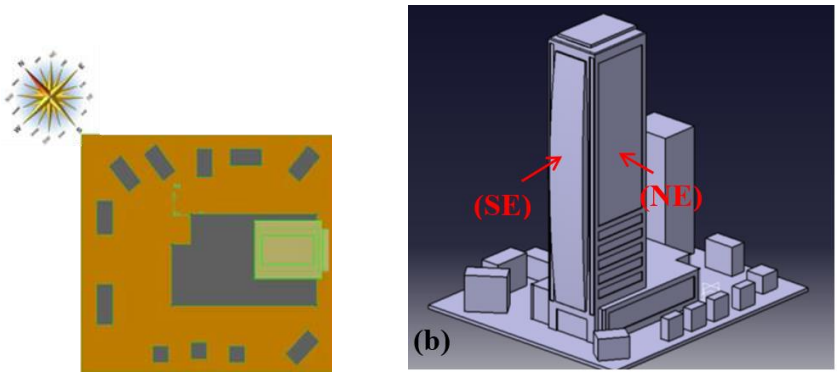

(a) (b)

Figure 1. Orientation of tall building model: (a) top view and (b) 3-D isometric view of the model

The turbulence intensity ratio is less than 0.5 %. In this kind of incompressible flows, Roberson and Crowe [25] reported that necessary similarity rule is the Reynolds number analogy between the model and prototype. Reynolds number is a non-dimensional number which relates dynamic effects to the viscous effects physically. It can be written as:

$$\mathrm{Re} = \frac{\rho V_\infty L}{\mu}, \tag{1}$$

where ρ is the density of the air, V_∞ is the free stream velocity, L is the characteristic length and μ is the dynamic viscosity. For prototype and model, Reynolds number analogy requires that:

$$(\mathrm{Re})_m = (\mathrm{Re})_p, \tag{2}$$

$$\frac{\rho_m (V_\infty)_m L_m}{\mu_m} = \frac{\rho_p (V_\infty)_p L_p}{\mu_p}, \tag{3}$$

Density and dynamic viscosity of the air can be considered as the same for model and prototype. Hence, $\rho_m = \rho_p$ and $\mu_m = \mu_p$. Dynamic viscosity is assumed as $\mu = 1.844 \times 10^{-5}\ \mathrm{kg/(ms)}$ and the following relation can be written:

$$(V_\infty)_m L_m = (V_\infty)_p L_p, \tag{4}$$

$$(V_\infty)_p = \frac{(V_\infty)_m L_m}{L_p} \tag{5}$$

Since $L_m / L_p = 144$, necessary wind velocity at test section of the wind tunnel reaches 144 times of the actual flow velocity, which results in an incredibly high speed of wind flow at test section. Reynolds numbers for the prototype and model are calculated considering characteristic lengths (L_m, L_p). These numbers are provided in Table 1.

Table 1. Reynolds number for the prototype and model at different cases

Case number	Wind speed [m/s]	$(\mathrm{Re})_m$	$(\mathrm{Re})_p$
Case-1	6	1.01 x 10^5	14.43 x 10^6
Case-2	12	2.03 x 10^5	28.86 x 10^6
Case-3	25	4.22 x 10^5	60.13 x 10^6

Reynolds number calculated for the scaled model is less than that for the prototype building. Maintaining incredibly high velocities in the tunnel section is almost impossible. Townsend [26] proposed that when Reynolds number exceeds a sufficiently high threshold, the flow regime will be non-dimensionally similar. Snyder [27] considered $\mathrm{Re} = 11000$ as a conservative threshold for the urban flow modeling with similar cube-like models. In the absence of thermal and Coriolis effects, the flow structure and turbulence are similar over a very wide range of Reynolds numbers, which has been used

extensively in modeling flow around sharped-edged geometry such as buildings or complex terrain [28]. In this case, although Reynolds number for the model is less than that of the prototype, useful $C_p - \mathrm{Re}$ relations are available for similar geometries in the literature to determine required wind velocity in the test section. C_p is the dimensionless pressure coefficient. $C_p - \mathrm{Re}$ graph provided in Roberson and Crowe [25] shows whether wind velocity in the tunnel section is adequate or not. Since Reynolds number is quite large, the flow around the building becomes turbulent as reported by Aygun and Baskaya [6]. When Reynolds number is greater than $0.5\text{x}10^5$, approximate viscous effect becomes minimal against inertial reaction, and there is almost no change on pressure coefficient $\left(C_p\right)$ with respect to Re number. For all the wind velocities given in Table 1, $\left(\mathrm{Re}\right)_m$ and $\left(\mathrm{Re}\right)_p$ is greater than 1.0×10^5. Despite the difference between Reynolds numbers of model and prototype, they could not affect the experimental results [25]. In this experiment, pressure values are measured by pressure tubes located on the surface of the model. In total, 45 pressure tubes are used in experiments. 15 pressure tubes are used on the surface of Side-A (SE), 14 pressure tubes are used on the surface of Side-B (NE), and 16 pressure tubes are used on the surface of Side-C (NE) with all spacing 4 cm between each other. In Figure 2, Side-A (SE), Side-B (NE) and Side-C (NW) are depicted with pressure tube location plan.

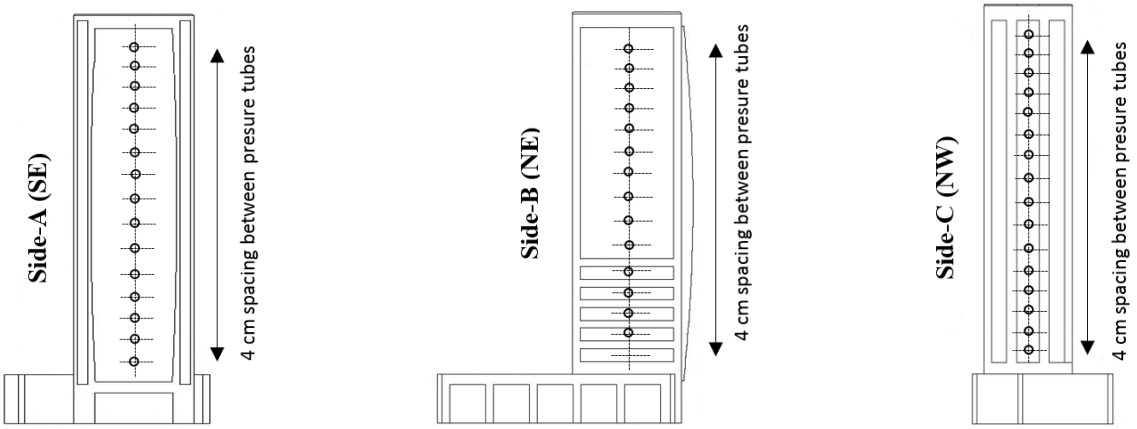

(a) (b) (c)

Figure 2. (a) Side-A (SE), (b) Side-B (NE) and (c) Side-C (NW) surfaces with pressure tube location plan

Wind stream is applied towards the Side-A (SE) surface of the model in the test section. Pressure tubes are connected to a multiple channel pressure transducer capable of measuring negative pressures. Each pressure tube is marked and jointed to the multiple channel pressure transducer by using flexible cyclones. Figure 3(a)-(d) respectively show general appearance of the mock-up model, pressure tube assemblage on the surface of model, connection of the marked cyclones to 64-channel pressure transducer, and wind stream direction in the test section.

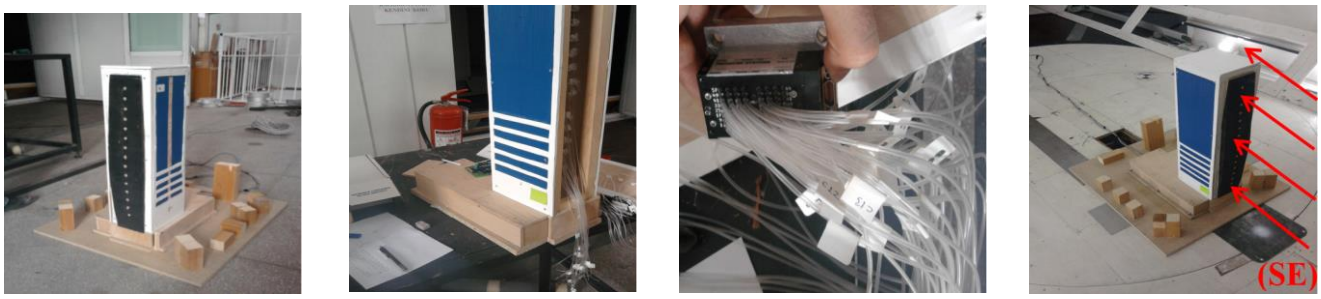

(a) (b) (c) (d)

Figure 3. (a) General appearance of the building model, (b) Pressure tube assemblage on the surface of model, (c) Connection of the cyclones to transducer and (d) Wind stream direction in the test section

2.2 Computational Fluid Dynamics (CFD) Approach

Computational model of the building was developed based on the scaled 3-D model. Different velocities of the wind flow through the Side-A (SE) were applied as velocity inlet boundary condition. Since flow around the building is turbulent, flow around the building should be examined considering turbulent flow conditions. Direct Numerical Simulation (DNS), Large-Eddy Simulation (LES) and Reynolds Averaging Navier Stokes (RANS) are main turbulence models that can be used in turbulent flow simulations [29]. While DNS and LES are more accurate tools in quantifying turbulent flow fields, these are quite expensive to be used for parametric study [30]. Hence, RANS is preferred and standard $k-\varepsilon$ turbulence model is used in flow analysis. Thermal effects are not taken into account, energy equation is

not considered. In this case, mass continuity, momentum in *x*,*y*,*z*-axes, and turbulence equations were solved iteratively. In incompressible flow case, these equations in computational domain can be written as follows [31–33]:

$$\frac{\partial \rho}{\partial t}+\frac{\partial(\rho u)}{\partial x}+\frac{\partial(\rho v)}{\partial y}+\frac{\partial(\rho w)}{\partial z}=0, \tag{6}$$

$$\rho\left(\frac{\partial u}{\partial t}+u\frac{\partial u}{\partial x}+v\frac{\partial u}{\partial y}+w\frac{\partial u}{\partial z}\right)=-\frac{\partial p}{\partial x}+\mu\left(\frac{\partial^2 u}{\partial x^2}+\frac{\partial^2 u}{\partial y^2}+\frac{\partial^2 u}{\partial z^2}\right)+\rho g_x, \tag{7}$$

$$\rho\left(\frac{\partial v}{\partial t}+u\frac{\partial v}{\partial x}+v\frac{\partial v}{\partial y}+w\frac{\partial v}{\partial z}\right)=-\frac{\partial p}{\partial y}+\mu\left(\frac{\partial^2 v}{\partial x^2}+\frac{\partial^2 v}{\partial y^2}+\frac{\partial^2 v}{\partial z^2}\right)+\rho g_y, \tag{8}$$

$$\rho\left(\frac{\partial w}{\partial t}+u\frac{\partial w}{\partial x}+v\frac{\partial w}{\partial y}+w\frac{\partial w}{\partial z}\right)=-\frac{\partial p}{\partial z}+\mu\left(\frac{\partial^2 w}{\partial x^2}+\frac{\partial^2 w}{\partial y^2}+\frac{\partial^2 w}{\partial z^2}\right)+\rho g_z, \tag{9}$$

where u, v, w are the x, y and z components of velocity vectors, p is the pressure, μ is the dynamic viscosity and ρ is the density of the fluid. g_x, g_y and g_z are the gravitational accelerations in cartesian coordinates. The equation for the turbulence kinetic energy (k) and dissipation (ε) based on the standard $k-\varepsilon$ turbulent model equations are provided in Eqs. (10)-(11) as follows [31–33]:

$$\frac{\partial}{\partial t}(\rho k)+\frac{\partial}{\partial x_i}(\rho k u_i)=\frac{\partial}{\partial x_i}\left[\left(\mu+\frac{\mu_t}{\sigma_k}\right)\left(\frac{\partial k}{\partial x_j}\right)\right]+P_k+P_b-\rho\varepsilon-Y_M+S_k, \tag{10}$$

$$\frac{\partial}{\partial t}(\rho\varepsilon)+\frac{\partial}{\partial x_i}(\rho\varepsilon u_i)=\frac{\partial}{\partial x_j}\left[\left(\mu+\frac{\mu_t}{\sigma_k}\right)\left(\frac{\partial k}{\partial x_j}\right)\right]+C_{1\varepsilon}\frac{\varepsilon}{k}(P_k+C_{3\varepsilon}P_b)-C_{2\varepsilon}\rho\frac{\varepsilon^2}{k}+S_\varepsilon, \tag{11}$$

where P_k is the generation of turbulence kinetic energy due to the mean velocity gradients and P_b is the generation of turbulence kinetic energy due to the buoyancy [31–33]. The term μ_t indicates turbulent viscosity as:

$$\mu_t=\rho C_\mu\frac{k^2}{\varepsilon}, \tag{12}$$

$$P_k=\mu_t S^2 \tag{13}$$

where S is the modulus of mean rate tensor which reads:

$$S=\sqrt{2S_{ij}S_{ij}}. \tag{14}$$

The term P_b can be calculated by,

$$P_b=\beta g_i\frac{\mu_t}{\mathrm{Pr}_t}\frac{\partial T}{\partial x_i} \tag{15}$$

where, Pr_t is the turbulent Prandtl number for energy and g_i is the component of the gravitational vector in the ith direction. For the standard and realizable $k-\varepsilon$ turbulence models, the default value of Pr_t is 0.85. β is the coefficient of thermal expansion, defined as:

$$\beta=-\frac{1}{\rho}\left(\frac{\partial\rho}{\partial T}\right)_P \tag{16}$$

Model constants are $C_{1\varepsilon}=1.44$, $C_{2\varepsilon}=1.92$, $C_\mu=0.09$, $\sigma_k=1.0$, $\sigma_\varepsilon=1.2$. Solution of Eq. (6)-(11) were carried out numerically based on Finite Volume Method (FVM) using ANSYS Fluent [34]. Turbulent flow was solved with the standard k-epsilon $(k-\varepsilon)$ turbulence model whose equations are given in Eqs. (10)-(11). Enhanced wall treatment was used to capture the boundary layer.

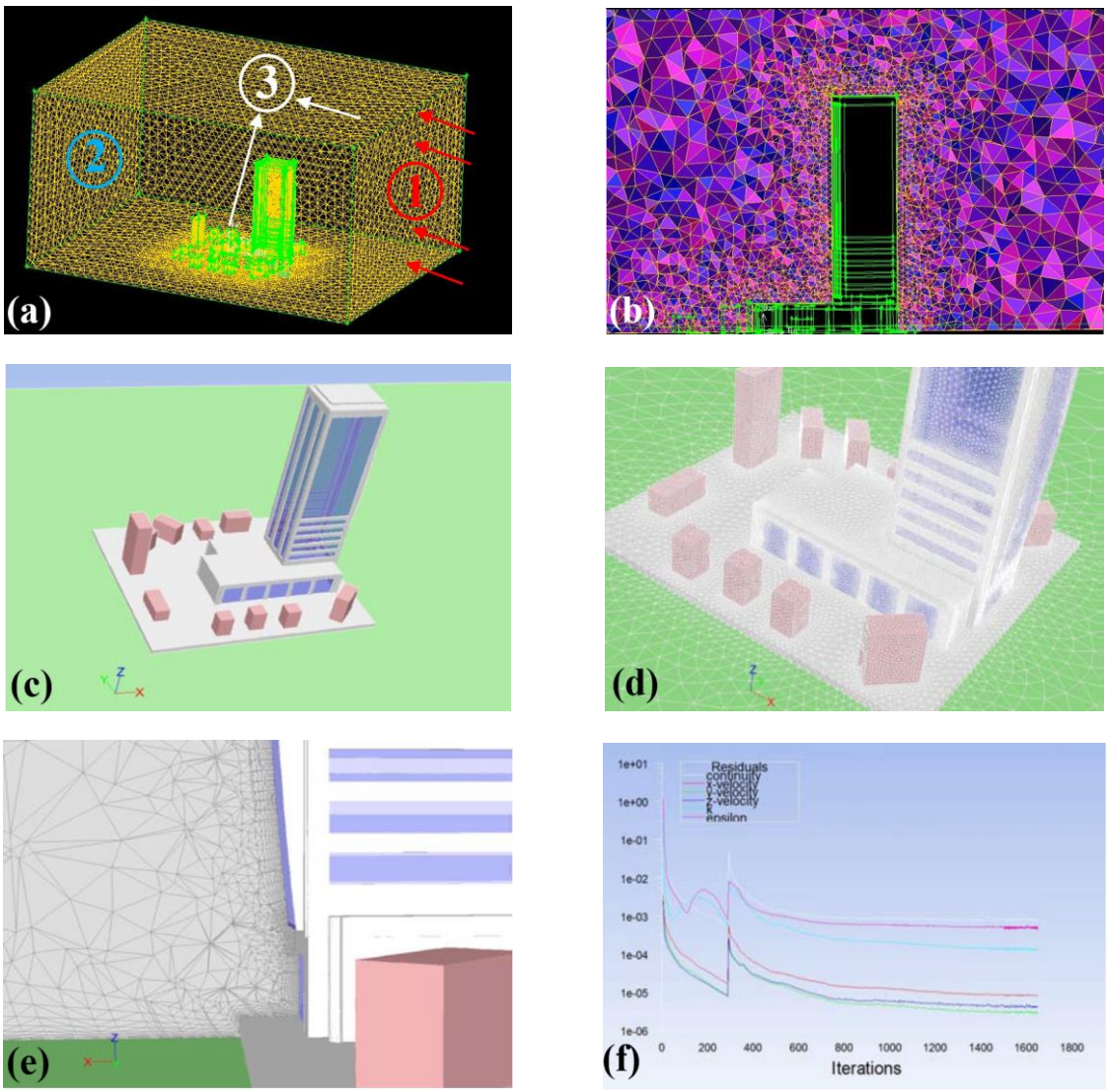

Figure 4. (a) Control volume and boundaryconditions, (b) Mesh distribution in control volume, (c) 3D building model, (d) Computational model with face mesh, (e) Boundary layer mesh on the surface of model and (d) Convergence history

The size of the finite volume mesh is adjusted to be fine enough to resolve the near-wall high gradients. To ensure the high-level similarities between numerical model and real prototype and to exclude impacts of blockage effects, the following requirement must be met during computational setting: blockage ratio should be less than 5% (Meng et al. [35]):

$$\delta = \frac{A_b}{A_{CD}} = 0.058. \tag{17}$$

where, δ is the blockage ratio, A_b is the area of the building wall perpendicular to the wind direction, A_{CD} is the area of the computational domain perpendicular to wind flow direction. $\delta = 0.058$ is quite less than 5% and satisfies the requirement. Figure 4(a) shows the control volume and the generated mesh. As computational mesh is determined, the grid independence study was carried out using computational model with different number of grids. Total number of mesh utilized in the model is around 1.7 million. It was observed that further increase in the grid number does not lead to considerable improvement, but it leads to require much computational power and time. The right face of control volume is labelled with 1 in a red color, indicating velocity inlet boundary condition, the left face is labelled with 2 in a blue color, denoting pressure outlet boundary condition, building faces and control volume boundaries are labelled with 3 in white, displaying stationary wall boundary condition. The mesh quality is important to acquire accurate solution. Hence, general guidelines called QRST (Quality, Resolution, Smoothness and Total cell count) was considered as adopted by Ozturk and Tari [36]. Quality of the mesh is adjusted automatically in ANSYS software considering skewness, aspect ratio and cell size. Smoothness in the mesh distribution is satisfied by assigning growth rate 15% from finer mesh to coarser mesh at control volume boundaries, as depicted in Figure 4(b). Mesh grids with blue and purple colors show high quality and those with red colors indicate lower quality grids. The 3D building model and the face mesh are depicted in Figure 4(c)-(d), respectively. The mesh in the boundary layer were prismatic and all the rest were tetrahedral as shown in Figure 4(e). Representative convergence history in CFD analysis is given in Figure 4(f) based on residuals of mass conservation,

momentum and $(k-\varepsilon)$ turbulence equations. Utilized fluid is air possessing properties as $\rho = 1.120\ kg/m^3$ at $P = 101.3\ kPa$ (atmospheric pressure) and $T = 300\ K$. The solution of Eq. (6)-(11) started by using 1st Order Upwind discretization since this method is an easier way for the convergence. However, this solution is interrupted at 300 iterations since this method does not provide very accurate results. Then, 2nd Order Upwind is employed to get more accurate results. As can be seen in Figure 4(f), all the residuals decreased below 10^{-3} at 1600 iterations, which indicates the precision of final results.

3.0 RESULTS AND DISCUSSION

3.1 Validation between Results of Experimental and Computational Methods

In order to validate the results of the developed computational method, pressure values obtained by experimental and computational methods were compared. The experimental data are acquired through the use of ESP 64HD Pressure Transducer as the averaging values of pressures obtained during wind tunnel testing. In the wind tunnel test, ten different pressure data were obtained with respect to time and these data were averaged to get the resultant pressure for each pressure tubes. Experiments were carried out at 6 m/s, 12 m/s and 25 m/s wind velocities. Pressure distributions on Side-A (SE), Side-B (NE) and Side-C (NW) are obtained for 6m/s, 12 m/s and 25 m/s wind stream velocities applied towards Side A (SE). Figure 5 depicts pressure distribution on different surfaces of the model for 6 m/s, 12 m/s and 25 m/s wind stream velocity. Figure 5(a)-(c) indicate the pressure distribution on Side-A for 6 m/s, 12 m/s and 25 m/s, respectively. While pressure level is around 23-25 Pa for 6 m/s, 72-78 Pa for 12 m/s, and 310-340 Pa for 25 m/s.

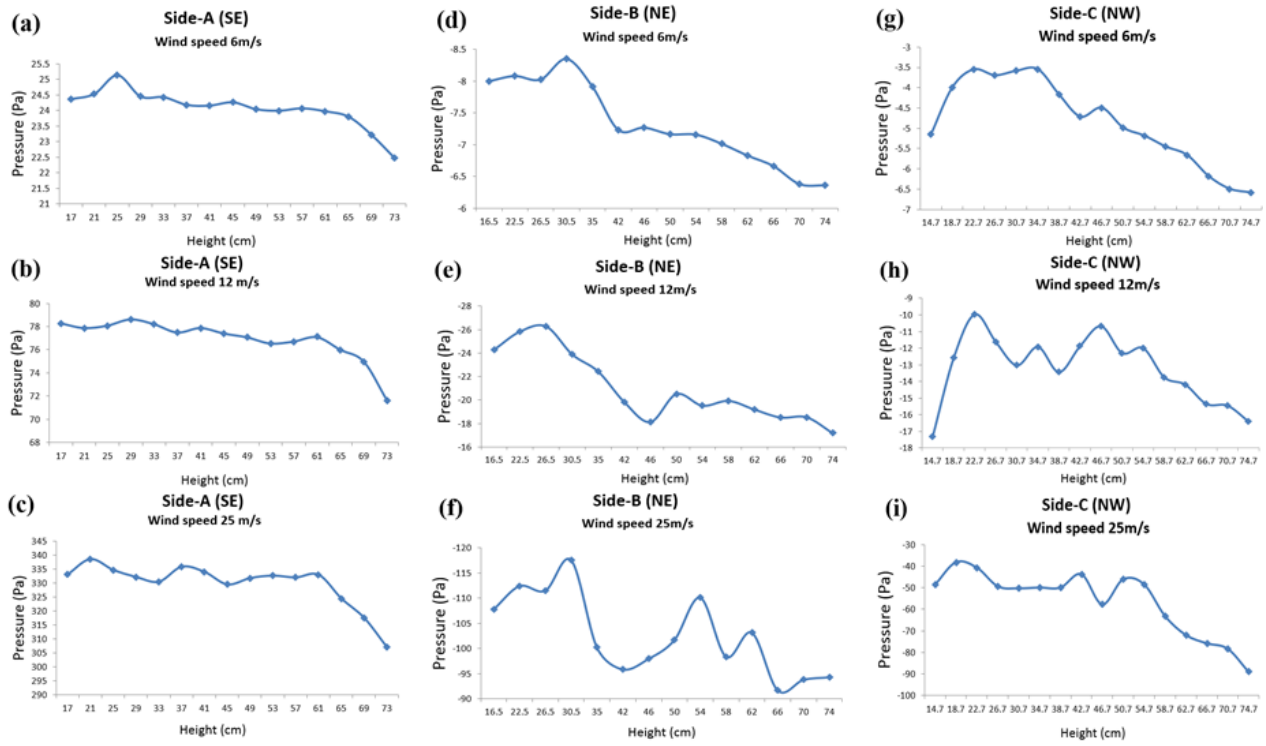

Figure 5. (a)-(c) Pressure distribution on Side-A (SE) for 6 m/s, 12 m/s and 25 m/s, (d)-(f) Pressure distribution on Side-B (NE) for 6 m/s, 12 m/s and 25 m/s, and (g)-(i) Pressure distribution on Side-C (NW) for 6 m/s, 12 m/s and 25 m/s

In addition, pressure levels at lower locations on Side-A (SE) of the building model is greater than those measured at higher points at uniform air strem condition. The main reason of this behavior is the compression of air due larger wall area existing in the building model, and hence occurrence of stagnation points especially on lower locations. Figure 5(d)-(f) show the pressure distribution on the surface of the Side-B. It is worthy to say that pressure values are negative which means suctions on this surface. Due to the suction, wind load is towards the outside. Pressure level is around negative 6-8 Pa for 6 m/s, negative 18-26 Pa for 12 m/s and negative 90-115 Pa for 25 m/s. Figure 5(g)-(i) demonstrate the pressure distribution on Side-C. Again, pressure values are negative on this surface. As the velocity of the stream is increased, the magnitude of the pressures is increased. At higher speeds of the stream, wavy behavior on the surface pressure exists especially on Side-B and Side-C due to irregular vortices emerging on these surfaces. Since air flow is towards Side-A (SE) direction, velocity of air becomes zero on Side-A, and there is a stagnation point on this surface. Pressure values on Side-A can be calculated theoretically using Bernoulli equation as follows:

$$P_{static} + \frac{1}{2}\rho_{air} V_{\infty}^{\ 2} = P_{stagnation} + \frac{1}{2}\rho_{air} V_{stagnation}^{\ 2} \tag{18}$$

Since $V_{stagnation} = 0$ and $P_{static} = 0$ in gauge pressure, the stagnation pressure can be written as:

$$P_{stagnation} = \frac{1}{2}\rho_{air} V_{\infty}^{2}. \tag{19}$$

Pressure values obtained for 6 m/s, 12 m/s and 25 m/s using Eq. (19) are found as 20.23 Pa, 80.93 Pa and 351.28 Pa as observed in Table 2. These values are used as a reference to calculate percent difference between experimental and theoretical (Difference^{E-T}) and that between computational and theoretical (Difference^{C-T}) pressure values. Experimentally, computationally and theoretically obtained pressure values on Side-A (SE) surface are close to each other. However, Difference^{E-T} is greater in all cases when it is compared to Difference^{C-T} due to mock-up surface quality and possible environmental disturbances during the experiment. Difference^{C-T} is quite small, which displays the accuracy of the computational method.

Table 2. Experimental, computational and theoretical pressure values on Side-A surface

Case number	Air flow velocity (V_{∞}) [m/s]	Pressure [Pa] (Experimental-avg.)	Pressure [Pa] (Computational-avg)	Pressure [Pa] (Theoretical)	Difference^{E-T} (%)	Difference^{C-T} (%)
Case-1	6	24.07	20.16	20.23	18.97	0.35
Case-2	12	76.70	80.10	80.93	5.22	1.02
Case-3	25	329.18	347.21	351.28	6.29	1.16

Figure 6 shows the pressure values with respect to height obtaineb by experimental and computational studies together for different uniform air flow velocity such as 6 m/s, 12 m/s and 25 m/s. It was observed that computational and experimental results are close to each other at lower velocities of air, and difference between these two results slightly increases at 25 m/s. The direction of the air flow is towards the Side-A (SE) of the building model, and obtained pressure values are taken from the Side-A (SE) surface. It can be said that experimentally and computationally obtained pressure values display a good agreement, which indicates the accuracy of the computational model.

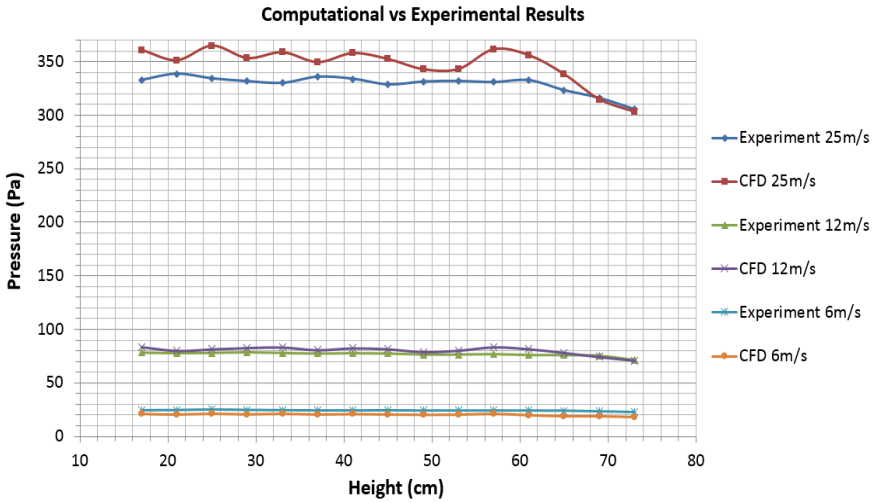

Figure 6. Effect of free stream velocity on the pressure values on the Side-A (SE) surface

After validation of the computational model, actual wind profile is modeled and building model is subjected to air flow with an increasing speed from the ground to higher elevation.

3.2 Actual Wind Profile Condition and Parametric Cladding Design

Actual wind velocity profile was determined and applied as a boundary condition for the computational model. Especially, for determination of the wind loads on tall buildings, the variation of the wind velocity from base to top point of the building has a considerable effect on accurate estimation of wind loads. The actual velocity profile can be expressed as a function of height. The mean wind speed velocity was expressed in the work conducted by Huang et al. [37, 38] in wind tunnel at Tong Ji (TJ) University, the wind velocity based on power-law function can be written as follows:

$$V_Z = V_R \times \left(\frac{H}{H_R}\right)^{\alpha} \tag{20}$$

where V_R is the reference wind speed, H_R is the reference height located 10m from the ground level and α is the exponential constant which was assumed as 0.35 in this study. Since building model is 1/144 scaled object of the actual prototype, actual wind profile in [0 100] m interval is scaled to [0 0.8] m for the model. Actual wind profile calculated

according to Eq. (20) is created as a velocity inlet boundary condition and this velocity distribution is illustrated on the black background in Figure 8(a). In Figure 8(b), pressure contours under actual wind profile condition are displayed on the building model. It is clear that the maximum pressure occurs towards the top of the Side-A surface. It is noteworthy to say that Side-B has blue regions of pressure contours along the model, which means negative pressure. Main reason of the occurrence of this blue region is the separation of the flow around the corners of the building model.

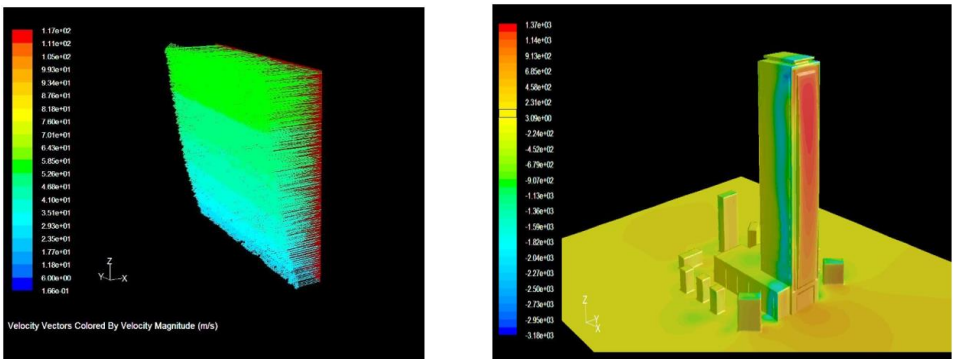

Figure 7. (a) Wind profile based on actual power-law method, (b) Pressure contours on building model subjected to actual wind profile

In Figure 8(a), actual wind profile is shown according to the prototype height. Computationally obtained pressures on Side-A (SE), Side-B (NE) and Side-C (NW) are provided, respectively. Pressure on Side-A is between 700-1400 Pa as provided in Figure 8(b). It is observed that pressure on Side-A is all positive and the maximum pressure appears around 60 cm from the bottom, around two-third of building height, which is consistent with the studies carried out by researchers Kikuchi et al. [39] and Hu et al. [40]. Figure 8(c) shows the pressure values on Side-B (NE). Pressure values are negative and it becomes maximum as ~ -2600 Pa around the top section (0.75m). Side-C (NW) has also negative pressure along the surface as illustrated in Figure 8(d), but magnitude of the negative pressure (~ -320 Pa) is lower at Side-C (NW) when compared to that of Side-B (NE). It is worthy to say that the magnitude of negative pressure distribution on side face (Side-B) is greater than that on the back side (Side-C), which was also found in Hu et al. [40].

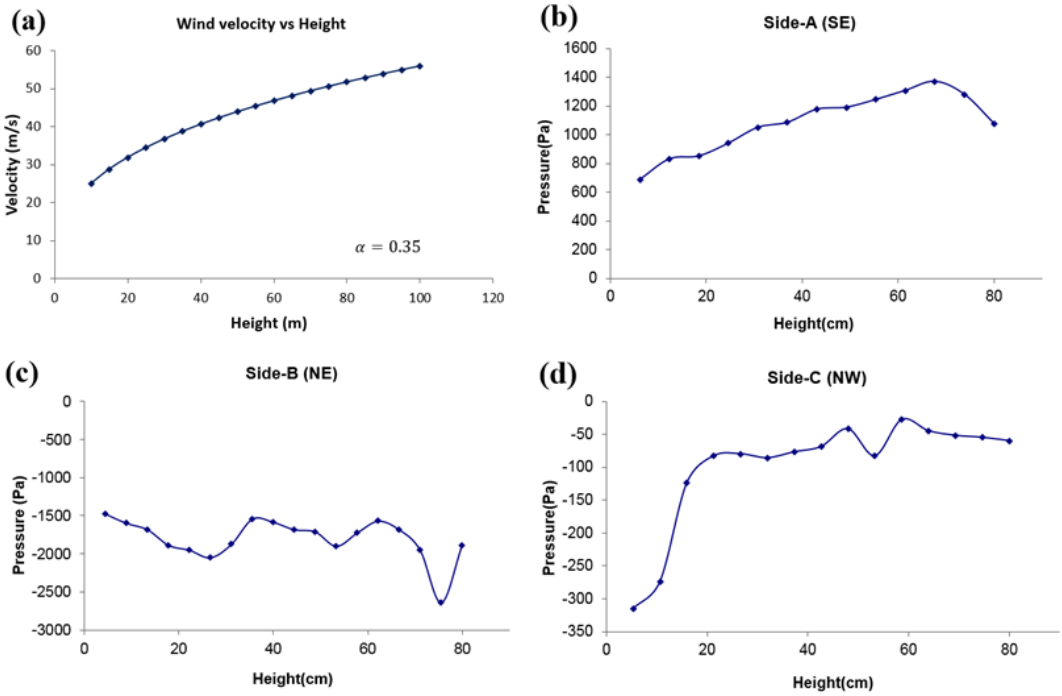

Figure 8. (a) Wind profile distribution with respect to height, (b) Pressure distribution on Side-A (SE) surface, (c) Pressure distribution on Side-B (NE) surface and (d) Pressure distribution on Side-C (NW) surface

In this section, new methodology is proposed for the selection and utilization of façade cladding elements. In conventional method, cladding elements are selected according to the maximum pressure that building subject to. Then, whole the building is constructed by cladding elements which can withstand this single critical pressure level. However, this approach will be conservative and leads to excessive construction material and cost due to the overdesign phenomenon. In this study, tall building model is divided into several zones called as Zone 1, Zone 2, Zone 3 and Zone 4. There are four zones in this study, but number of zones can be adjusted by user, parametrically. New parametric design method allow designer to select different cladding elements for different zones. Although wind stream direction has a

considerable effect, considered zones are insensitive to wind direction due to safety considerations. Critical pressure level for each zone is recorded and load carrying cladding elements are selected to withstand this critical pressure. Figure 9(a)-(e) depicts wind profile, building model with different zones involving cladding elements, load carrying beams with glass assembly, load carrying beams and beam cross-section, respectively.

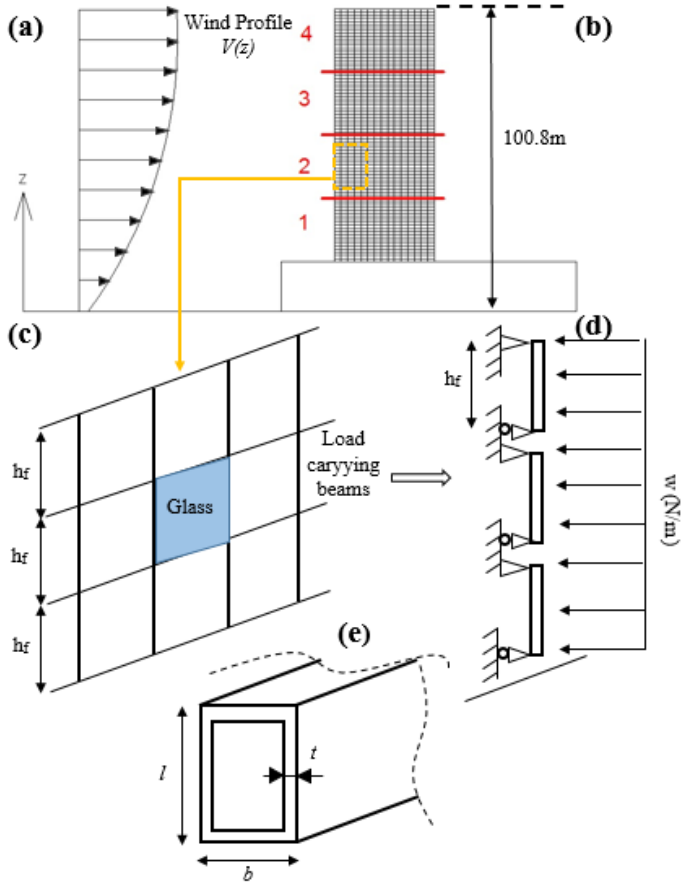

Figure 9. Schematics of parametric design for cladding structures, (a) Actual wind profile based on power-law, (b) Building with prescribed zones, (c) Load carrying beam structures with glass assembly, (d) Load carrying beams under wind load and (e) Cross-section of load carrying beams

Total height of the tall building is 100.8 m except the roof section. Building prototype is divided into four different zones from ground to top floor. Hence, each zone includes 25.2 meters. The height of each floor is 2.8m. Since floor height is 2.8m, the height of the load carrying beam and glass window is assumed as $h_f = 2.8\,m$, respectively. Correspondingly, each zone involves 9 floors. b, l and t respectively denote width, length and wall thickness of the beam. Aluminum alloy is widely used in the construction of cladding of tall buildings [41, 42]. Hence, material of the load carrying beams are considered as aluminum alloy. Properties of utilized aluminum alloy is given in Table 3.

Table 3. Properties of aluminum alloy 6061-T4 [43]

Property	Value
Elastic Modulus (GPa) E	68.9
Density (kg/m^3) ρ	2700
Yield Strength (MPa) S_Y	145
Tensile Strength (MPa) S_{UT}	241

Wind load applied to each load carrying beam in glass-wall cladding system is calculated as follows:

$$w = \left(p_{critical}\right)^{Zone\,(i)} \cdot b \quad [\mathrm{N/m}], \tag{21}$$

where $\left(p_{critical}\right)^{Zone\,(i)}$ is the critical pressure of the Zone (i). Values of critical pressure on different surfaces of the model is recorded and provided in Table 4. While determining critical pressure in each zone, the maximum pressure is taken regardless of the sides of the building since wind stream velocity may change in real cases. It can be seen in Table 4 that pressures values acquired on Side-B and Side-C are negative while pressure values on Side-A is positive since this face is subjected to direct wind stream. Same conclusion was drawn from the study conducted by Aygun and Baskaya [6]. It

is crucial to state that the magnitude of negative pressures on Side-B are greater than that obtained on Side-C. Thus, critical pressure values are recorded from Side-B. The maximum negative pressure is observed at Zone 4 on Side-B.

Table 4. Critical pressure values for four different zones

Zone/Direction	Zone 1 [0 25.2] m	Zone 2 [25.2 50.4] m	Zone 3 [50.4 75.6] m	Zone 4 [75.6 100.8] m
	$\left(p_{critical}\right)^{Zone\ (1)}$	$\left(p_{critical}\right)^{Zone\ (2)}$	$\left(p_{critical}\right)^{Zone\ (3)}$	$\left(p_{critical}\right)^{Zone\ (4)}$
Side-A (SE)	851.4 Pa	1176 Pa	1307 Pa	1370 Pa
Side-B (NE)	-1885 Pa	-2048 Pa	-1898 Pa	-2640 Pa
Side-C (NW)	-315 Pa	-86 Pa	-83 Pa	-60 Pa
Critical	-1885 Pa	-2048 Pa	-1898 Pa	-2640 Pa

The minimum negative pressure is obtained at Zone 4 on Side-C. Since critical pressures are negative for the building model, it is required to design load carrying beams according to these negative pressures instead of positive pressures seen on Side-A. Figure 10 shows the flowchart for parametric design of cladding structures. In order to show the usefulness of the developed parametric method, simple box type beams are considered. Cross-section and moment of inertia for box type beams are calculated as follows:

$$A_c = bl-(b-t)(l-t), \tag{22}$$

$$I = I_1 - I_2 = \frac{1}{12}\left(bl^3-(b-t)(l-t)^3\right). \tag{23}$$

In calculations, width of the load carrying beams are assumed constant as $b = 0.03\text{m}$. The maximum allowable deflection for the glass-wall cladding system withstanding maximum wind pressure of 2400 Pa was reported as 50 mm [44]. The American Architectural Manufacturers Association addresses deflection in its standard AAMA TIR-11 Maximum Allowable Deflection of Framing Systems for Building Cladding Components at Design Wind Loads, and it was determined as $h_f/175 = 16\,\text{mm}$ for spans less than 13ft 6 inches [45]. Hence, maximum deflection is taken as 20 mm in calculations, which falls the specified interval.

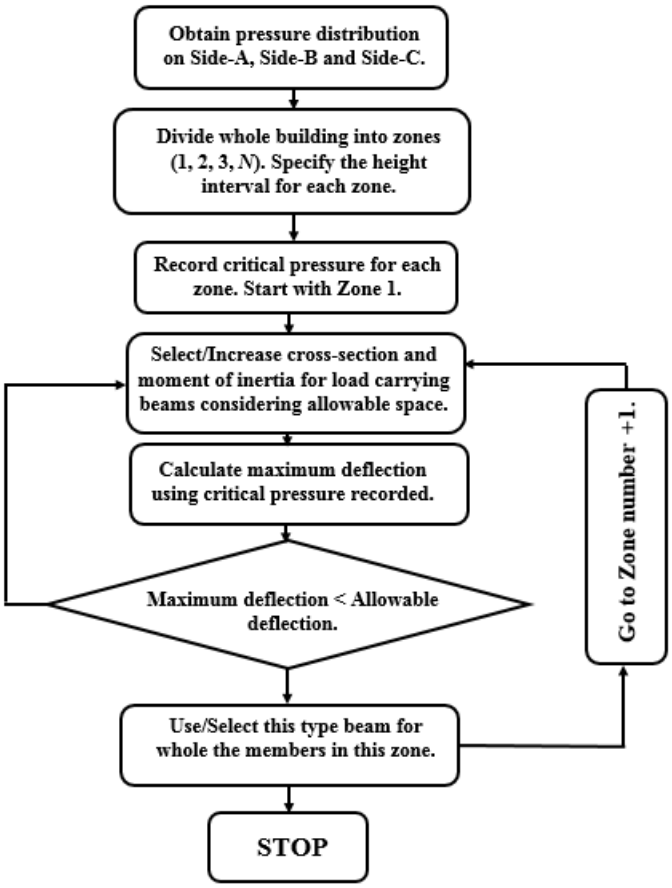

Figure 10. Flowchart of the developed parametric load carrying beam selection according to the wind pressure

In calculations, the wall thickness is varied between 0mm to 3mm for Zone 1, Zone 2, Zone 3 and Zone 4. Maximum deflection, slopes at ends, maximum moment and stress are calculated based on the simply-supported beam equations as follows [46]:

$$y_{\max} = -\frac{5\, w \left(h_f\right)^3}{24\, E\, I}, \tag{24}$$

$$\theta_A = \frac{w \left(h_f\right)^3}{24\, E\, I}, \quad \theta_B = -\theta_A, \tag{25}$$

$$M_{\max} = \frac{w \left(h_f\right)^2}{8} \quad @\left(x = h_f/2\right), \tag{26}$$

$$\sigma_{\max} = \frac{M_{\max}\left(l/2\right)}{I}. \tag{27}$$

When parametric method given in Figure 10 is applied to the problem, minimum wall thickness for each zone is found by solution of Eqs. (24)-(27) in Matlab. These minimum allowable thickness values are marked for four different zones in Figure 11(a)-(d). The allowable deflection was marked as 20 mm at vertical axis and corresponding thickness value was determined for different zones. While wall thickness for Zone 1 and Zone 3 are 1.5 mm, that for Zone 2 and Zone 4 are 1.7mm and 2.3mm, respectively.

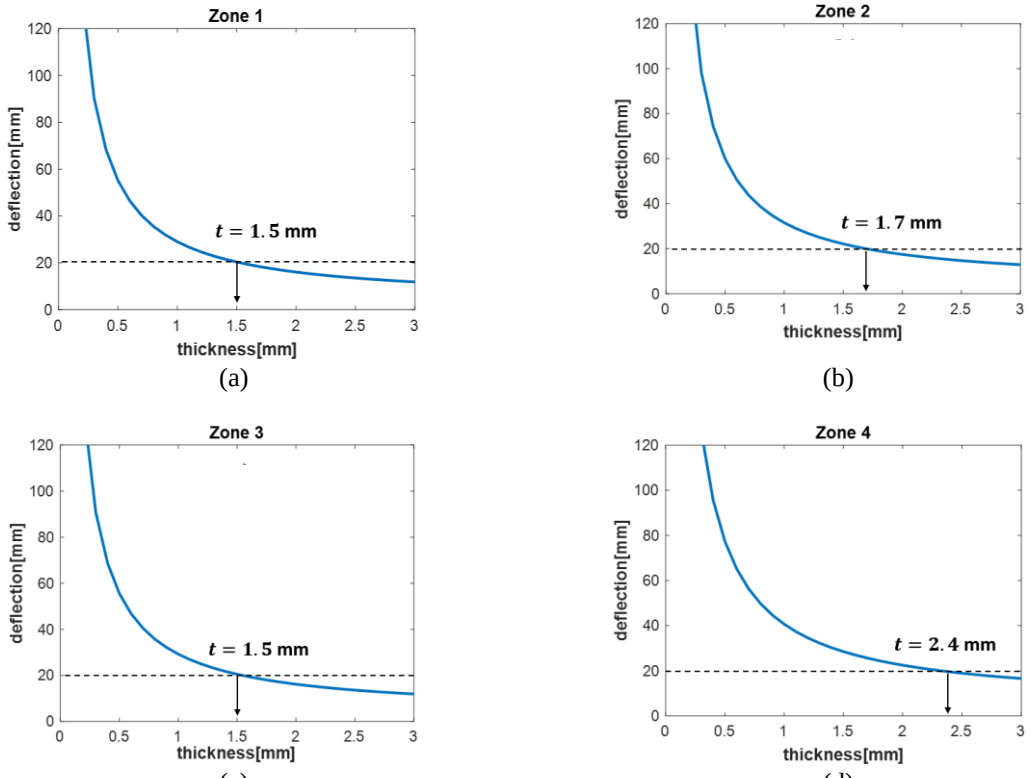

Figure 11. Minimum allowable thickness values for the load carrying beams $b = 30\,\text{mm}$, $l = 30\,\text{mm}$ for (a) Zone 1, (b) Zone 2, (c) Zone 3, (d) Zone 4

Wall thickness of the load carrying elements are determined parametrically based on the pressure results acquired from CFD analysis. Since critical pressures are negative in design of cladding structures, load is applied from inside to outside during wind flow. Table 5 illustrates critical pressure for each zone $\left(p_{critical}\right)^{Zone\,(i)}$, moment of inertia of selected beams $\left(I\right)$, slope at ends in degrees $\left(\theta_A, \theta_B\right)$, maximum stress on beams $\sigma_{\max}$, and total number of load carrying beams at each zone $\left(k\right)$. The mass of each beam can be calculated as:

$$m_b = \rho_{Al6061}\, A_c\, h_f. \tag{28}$$

Since each zone is assumed to involve k number load carrying beams, total mass of aluminum beams for each zone is:

$$M^{Zone(i)} = m_b\, k. \tag{29}$$

Table 5. Results of mechanics analysis for parametric cladding system design

	Parametric design based on CFD (Maximum allowable deflection: 20mm)						Conventional design based on maximum pressure
	Critical pressure [Pa]	Moment of Inertia (I) $\times 10^{-6}$ m^4	Slope at ends (degree)	Max. Stress $\sigma_{\max}$ (MPa)	Number of load carrying beams (k)	Mass (kg) $M^{Zone(i)}$	Mass (kg) $M^{Zone(i)}$
Zone 1	-1885	0.02321	$\theta_A = -1.8291$ $\theta_B = 1.8291$	71.62	1242	1605.61	2487.84
Zone 2	-2048	0.02578	$\theta_A = -1.7894$ $\theta_B = 1.7894$	70.07	1242	1806.94	2487.84
Zone 3	-1898	0.02321	$\theta_A = -1.8417$ $\theta_B = 1.8417$	72.12	1242	1706.94	2487.84
Zone 4	-2640	0.03389	$\theta_A = -1.7544$ $\theta_B = 1.7544$	68.70	1242	2487.84	2487.84
Total Mass (kg)						7607.3	9951.4

Total aluminum material used for each zone was calculated based on the critical pressure obtained in CFD analysis in parametric way. In addition to that, total mass of aluminum cladding mass based on single critical pressure in a conventional way was calculated. In conventional way, there is no zone in the building and whole building was constructed by aluminum beams which can withstand -2640 Pa. Hence, utilized mass of aluminum in conventional way is greater than that obtained parametric method based on CFD. Moreover, safety factor for the load carrying beams at each zone can be calculated using Eq. (30):

$$SF^{Zone(i)} = S_Y / \sigma_{\max}. \tag{30}$$

Table 6. Safety factors for cladding elements utilized in each zone

Safety factor/Zone	Zone 1	Zone 2	Zone 3	Zone 4
$SF^{Zone(i)}$	2.03	2.07	2.01	2.11

These results indicate that parametric cladding selection provides 23.6% less aluminum material usage without lowering the safety factor of 2.0 at each zone. If conventional approach was used, safety factor for each zone would be different and much greater for low pressure zone. Thus, safety factor for the cladding of whole building is maintained around 2.0 for each zone based on this method.

4.0 CONCLUSIONS

This study puts forward a new parametric method for cladding structure design for tall buildings. In conventional method, cladding structures are designed according to the single maximum pressure obtained in wind load analysis, and all cladding elements are selected based on this single pressure. Hence, overdesign and execessive material usage is undeniable. However, in this method, whole building is divided into zones from ground to top and critical pressures for each zone is recorded by means of computational fluid dynamics (CFD) approach. Cladding structures are designed parametrically based on the critical pressures belonging to each zone. Hence, this parametric method enables designer to use different kind of elements for each zone in a flexible way, hence it provides significant economy on material usage and construction costs. Following conclusions can be drawn from this study:

- Tall building prototype was selected and its scaled model was manufactured considering wind tunnel test section. Building model was subjected to uniform wind stream in experimental analysis and computational analysis. It was shown that experimental and computational results were in good agreement at different wind flow velocities. The maximum difference between computational and experimental results were around 18%. Difference between results may arise from surface quality of mock-up model.
- In uniform wind stream, although pressure values on the surface of Side-A (SE) was positive, those obtained on Side-B (NE) and Side-C (NW) surfaces were negative, which means suction at those surfaces.

- In experiments, as air flow velocity was increased, the magnitude of pressures on each surface was increased. Moreover, theoretical surface pressures were calculated on Side-A using Bernoulli equation. It was observed that experimental, computational and theoretical pressure values were close to each other, which demonstrates the accuracy of the computational model.
- Once validation of the computational model was achieved, actual wind profile was generated based on the power-law function. This wind profile was scaled to model dimensions and applied to the model as a velocity inlet boundary condition. Since air velocity was increased at higher elevations, greater pressure values were obtained. Although values of positive pressures were higher at top section of Side-A (SE), the magnitude of negative pressures were greater on Side-B (NE) surface due to the vortices arising in the sharp corners of the model. Thus, critical design pressures were negative, which leads to wind load from inside to outside.
- Cladding structure design was performed parametrically at different zones considering maximum allowable deflection of glass-wall cladding systems based on strength calculations. The developed parametric method provided 23.6% less material usage without lowering the factor of safety throughout the building. Utilization of less construction material reduces the carbon footprint and saves the environment. Hence, developed methods can be used for cladding system design of tall buildings for minimization of construction material and cost.

5.0 ACKNOWLEDGEMENTS

Authors are thankful to TUBITAK-SAGE (The Scientific and Technological Council of Turkey) for letting them use of the Ankara Wind Tunnel (AWT), to Ankara Aluminyum for giving information about outer dimensions of the tall building model. Authors would like to thank Emre Öztürk at Anova Engineering Ltd. for the technical supervision during tests and analysis.

6.0 REFERENCES

[1] J. D. Holmes, C. Paton, and R. Kerwin, *Wind loading of structures*, 2nd Ed. New York, USA: Taylor & Francis, New York, USA, 2007.

[2] A. R. Barriga, C. T. Crowe, and J. A. Robertson, "Pressure distribution on a square cylinder at a small angle of attac in a turbulent cross flow," *Proceedings of the Fourth International Conference on Wind Effects on Buildings and Structures*, London, United Kingdom, 1977, pp. 89–164.

[3] J. A. Roberson and C. T. Crowe, "Pressure distribution on model buildings at small angles of attack in turbulent flow," in *In. Proceedings, the third U.S. National Conference on Wind Engineering Research*, University of Florida, Gainesville, 1978, pp. 289–292.

[4] J. E. Cermak, "Wind-tunnel development and trends in applications to civil engineering," *Journal of Wind Engineering and Industrial Aerodynamics*, vol. 91, no. 3, pp. 355–370, 2003.

[5] S. Ahmad and K. Kumar, "Effect of geometry on wind pressures on low-rise hip roof buildings," *Journal of Wind Engineering and Industrial Aerodynamics*, vol. 90, no. 7, pp. 755–779, 2002.

[6] C. Aygun. and S. Baskaya, "An experimental study of surface pressure distribution of a high rise building formed by wind flow," *Journal of the Faculty of Engineering and Architecture of Gazi University*, vol. 18, no. 4, pp. 15–31, 2003.

[7] Y. Kim and J. Kanda, "Characteristics of aerodynamic forces and pressures on square plan buildings with height variations," *Journal of Wind Engineering and Industrial Aerodynamics*, vol. 98, no. 8–9, pp. 449–465, 2010.

[8] N. Lin, C. Letchford, Y. Tamura, B. Liang, and O. Nakamura, "Characteristics of wind forces acting on tall buildings," *Journal of Wind Engineering and Industrial Aerodynamics*, vol. 93, no. 3, pp. 217–242, 2005.

[9] F. Cluni, V. Gusella, S. M. J. Spence, and G. Bartoli, "Wind action on regular and irregular tall buildings: Higher order moment statistical analysis by HFFB and SMPSS measurements," *Journal of Wind Engineering and Industrial Aerodynamics*, vol. 99, no. 6–7, pp. 682–690, 2011.

[10] J. Xie, "Aerodynamic optimization of super-tall buildings and its effectiveness assessment," *Journal of Wind Engineering and Industrial Aerodynamics*, vol. 130, pp. 88–98, 2014.

[11] N. Isyumov, E. Ho, and P. Case, "Influence of wind directionality on wind loads and responses," *Journal of Wind Engineering and Industrial Aerodynamics*, vol. 133, pp. 169–180, 2014.

[12] H. Tanaka, Y. Tamura, K. Ohtake, M. Nakai, and Y. Chul Kim, "Experimental investigation of aerodynamic forces and wind pressures acting on tall buildings with various unconventional configurations," *Journal of Wind Engineering and Industrial Aerodynamics*, vol. 107–108, pp. 179–191, 2012.

[13] Y. C. Kim, S. W. Yoon, D. J. Cheon, and J. Y. Song, "Characteristics of wind pressures on retractable dome roofs and external peak pressure coefficients for cladding design," *Journal of Wind Engineering and Industrial Aerodynamics*, vol. 188, pp. 294–307, 2019.

[14] G. Pomaranzi, N. Daniotti, P. Schito, L. Rosa, and A. Zasso, "Experimental assessment of the effects of a porous double skin façade system on cladding loads," *Journal of Wind Engineering and Industrial Aerodynamics*, vol. 196, p. 104019, 2020.

[15] N. H. Wong and H. K. Chin, "An evaluation exercise of a wind pressure distribution model," *Energy and Buildings*, vol. 34, no. 3, pp. 291–309, 2002.

[16] H. Montazeri and B. Blocken, "CFD simulation of wind-induced pressure coefficients on buildings with and without balconies: Validation and sensitivity analysis," *Building and Environment*, vol. 60, pp. 137–149, 2013.

[17] E. Reda, R. Zulkifli, and Z. Harun, "Towards developing an idealised city model with realistic aerodynamic features," *Journal of Mechanical Engineering and Sciences*, vol. 11, no. 4, pp. 2979–2992, 2017.

[18] C. McGuill and J. Keenahan, "A parametric study of wind pressure distribution on façades using computational fluid dynamics," *Applied Sciences*, vol. 10, no. 23, p. 8627, 2020.

[19] M. F. Ciarlatani, Z. Huang, D. Philips, and C. Gorlé, "Investigation of peak wind loading on a high-rise building in the atmospheric boundary layer using large-eddy simulations," *Journal of Wind Engineering and Industrial Aerodynamics*, vol. 236, p. 105408, 2023.

[20] P. Mendis, T. Ngo, N. Haritos, A. Hira, B. Samali, and J. Cheung, "Wind loading on tall buildings," *Electronic Journal of Structural Engineering*, vol. 7, pp. 41–54, 2007.

[21] J. E. Cermak *et al.*, "Wind tunnel studies of buildings and structures," *American Society of Civil Engineers*, Reston, Virginia, 1999.

[22] A. Dagnew and G. T. Bitsuamlak, "LES evaluation of wind pressures on a standard tall building with and without a neighboring building," in *The Fifth International Symposium on Computational Wind Engineering (CWE2010)*, Chapel Hill, North Carolina, USA, 2012.

[23] B. Kayışoğlu, Ö. Kurç, and O. Uzol, "Estimation of wind loads on tall buildings through wind tunnel testing," in *10th International Congress on Advances in Civil Engineering*, Ankara, Turkey, 2012.

[24] E. Simiu and R. H. Scanlan, *Winds Effects on Structures: Fundamentals and Applications to Design*. 3rd Ed. John Wiley & Sons, New York, 1996.

[25] J. A. Roberson and C. T. Crowe, *Engineering Fluid Mechanics*, 2nd Ed. Boston, USA: Houghton Mifflin Company, 1980.

[26] A. A. R. Townsend, *The Structure of Turbulent Shear Flow*, 2nd Ed. Cambridge: Cambridge University Press, 1980.

[27] W. H. Snyder, "Research and Development: Guideline for Fluid Modeling of Atmospheric Diffusion," *United States Environmental Protection Agency*, 1981.

[28] M. M. Orgill, "Critical review of wind tunnel modeling of atmospheric heat dissipation," *Energy Research and Development Administration*, Constract no. EY-76-C-06-1830, 1977.

[29] M. Barbason and S. Reiter, "About the choice of a turbulence model in building physics simulations," in *7th Conference on Indoor Air Quality, Ventilation and Energy Conservation in Buildings (IAQVEC 2010)*, Syracuse, NY, United States, 2010, pp. 1–8.

[30] N. Kumar, V. K. Chalamalla, and A. Dewan, "Reynolds-Averaged Navier-Stokes modeling of a turbulent forced plume in a stratified medium," *Materials Today: Proceedings*, vol. 47, pp. 3068–3072, 2021.

[31] J. E. Bardina, P. G. Huang, and T. J. Coakley, "Turbulence modeling validation, testing, and development," *NASA Technical Memorandum*, no. 110446, 1997.

[32] W. P. Jones and B. E. Launder, "The prediction of laminarization with a two-equation model of turbulence," *International Journal of Heat and Mass Transfer*, vol. 15, no. 2, pp. 301–314, 1972.

[33] D. C. Wilcox, *Turbulence Modeling for CFD*, 2nd Ed. Anaheim: DCW Industries, 1998.

[34] "ANSYS Inc." ANSYS Fluent 12.0 Documentation, 2009.

[35] F. Q. Meng, B. J. He, J. Zhu, D. X. Zhao, A. Darko, and Z. Q. Zhao, "Sensitivity analysis of wind pressure coefficients on CAARC standard tall buildings in CFD simulations," *Journal of Building Engineering*, vol. 16, pp. 146–158, 2018.

[36] E. Ozturk and I. Tari, "CFD modeling of forced cooling of computer chassis," *Engineering applications of computational fluid mechanics*, vol. 1, no. 4, pp. 304–313, 2007.

[37] P. Huang, P. Luo, and M. Gu, "Pressure and forces measurements on CAARC standard Tall building in wind tunnel of Tong Ji University," in *Proceedings of the 12th National Wind Engineering Conference of China*, Xi'an, 2007, pp. 240–244.

[38] S. Huang, Q. S. Li, and S. Xu, "Numerical evaluation of wind effects on a tall steel building by CFD," *Journal of Constructional Steel Research*, vol. 63, no. 5, pp. 612–627, 2007.

[39] H. Kikuchi, Y. Tamura, H. Ueda, and K. Hibi, "Dynamic wind pressures acting on a tall building model — proper orthogonal decomposition," *Journal of Wind Engineering and Industrial Aerodynamics*, vol. 69–71, pp. 631–646, 1997.

[40] G. Hu, J. Song, S. Hassanli, R. Ong, and K. C. S. Kwok, "The effects of a double-skin façade on the cladding pressure around a tall building," *Journal of Wind Engineering and Industrial Aerodynamics*, vol. 191, pp. 239–251, 2019.

[41] V. Dréan, B. Girardin, E. Guillaume, and T. Fateh, "Numerical simulation of the fire behaviour of facade equipped with aluminium composite material-based claddings-Model validation at large scale," *Fire and Materials*, vol. 43, no. 8, pp. 981–1002, 2019.

[42] M. A. Kamal, "Recent advances in material science for facade systems in contemporary architecture: An overview," *American Journal of Civil Engineering and Architecture*, vol. 8, no. 3, pp. 97–104, 2020.

[43] "Al alloy 6061-T4 properties." Accessed: Aug. 10, 2021. [Online]. Available: www.matweb.com

[44] "The design-assist approach to affordable 'jewel' façades." [Online]. Available: https://www.constructionspecifier.com/the-design-assist-approach-to-affordable-jewel-facades/3/

[45] "2018 Codes Clarify Deflection Limits for Glass Wall Systems." [Online]. Available: https://www.glassmagazine.com/article/2018-codes-clarify-deflection-limits-glass-wall-systems

[46] F. P. Beer, E. R. Johnston Jr, J. T. Dewolf, and D. F. Mazurek, *Mechanics of Materials*, 6th Ed. New York, USA: Mc Graw Hill, 2012.